International Journal of Computer Information Systems and Industrial Management Applications
ISSN 2150-7988 Volume 18(14s) 2026 pp. 961-975
https://doi.org/10.70917/ijcisim-2026-4305
Article

Security-Aware Spectral Amplitude Coding for High-Speed OCDMA Networks: Full-Resolution SSFM Validation and Direct Operating-Boundary Optimization

M. M. Shukra[1] and *G. Prathibha[1]

[1]Department of Electronics and Communication Engineering, Acharya Nagarjuna University, Nagarjuna Nagar, Andhra Pradesh, India
ORCID IDs: Mohamed Shukra https://orcid.org/0009-0005-6618-2753
G. Prathibha https://orcid.org/0000-0001-7827-3736

Abstract: Security in spectral-amplitude-coding optical code-division multiple access (SAC-OCDMA) is often inferred from code obscurity, even though a code that suppresses multiuser interference may still be learnable by an unauthorized receiver. We examined this issue through a security-aware SAC (SA-SAC) link in which the wavelength assignment changes with a secret key and time index while the users retain disjoint spectral supports. The reference system used $L = 64$, $K = 16$, $w = 4$, and 10 Gb/s per user. Its analytical Bob–Eve model was checked against a 27-point, full-resolution split-step Fourier method (SSFM) grid covering three fiber conditions, three distances, and launch powers of −6, 4, and 12 dBm/user. Every point was rerun with $dz \leq 0.125$ km, 64 bits, and spectral oversampling of 3, the receiver also compensated the wavelength-dependent chip delays before detection. The 12 dBm/user rows behaved as a separate nonlinear-stress regime and were not used to fit the operating-region correction.
For the remaining 18 rows, ridge calibration reduced Q-RMSE from 10.421 to 2.5624 and changed $Q - R^2$ from −0.3904 to 0.9159. A quadratic-ridge model ($\lambda = 0.001$) gave a leave-one-distance-out Q-RMSE of 4.3427, but its uncertainty interval was too broad for a defensible boundary claim. We therefore used the model only to choose 14 additional distance cases and six power cases for direct SSFM evaluation. With $Q_{SSFM} \geq 6$ and $ILR \leq 0.05$ bit/symbol, the last tested feasible points were 65 km at 4 dBm/user for standard SMF, 50 km at 3 dBm/user for dense WDM, and 70 km at 4 dBm/user for the low-dispersion case. Their Q-factors were 6.3786, 6.2473, and 6.8981, and the modeled ILR was zero in each case. The MATLAB workflow was checked by 132 unit and integration tests. The main outcome is a directly verified set of operating brackets, together with an explicit distinction between the region that was calibrated and the high-power region in which the analytical approximation failed.
Keywords: SAC-OCDMA, physical-layer security, information leakage rate, split-step Fourier method, fiber nonlinearities, region-aware calibration. direct boundary validation, power optimization.

1. Introduction

Optical code-division multiple access (OCDMA) offers asynchronous access and code-domain user separation without requiring all transmitters to share a common clock. OCDMA(Spectral-Amplitude-Coding) corresponding of user is done by a set of wavelength chips. Decoding is done by matching the spectral pattern at the receiver. The recent works have focused on bigger code families, lower correlations, more polarization or spatial dimensions, and improved receiver structures [1–8]. These advancements boost capacity or diminish multiaccess interference. However, none of these advancements alone measure what an eavesdropper can deduce from the transmitted spectrum.

Efforts towards secure OCDMA have taken a different route. Several studies have explored secrecy capacity, eavesdropper error, or information leakage [1,5,9,10], however, propagation-oriented ones usually report Q-factor or BER for the legitimate receiver [4-8,11]. In a single model, it is rare for the two sources of evidence to overlap. Similarly, the use of machine-learning applications in optical networks is now commonplace for predicting quality-of-transmission, monitoring, and equalization [12–16]. However, confidentiality is rarely included in the rules used to select an operating point. This separation matters because a link can be reliable for Bob and still leak useful structure to Eve.

The discrepancy worsens as the speed increases to . Chromatic dispersion causes the wavelengths of chips to shift over time, while Kerr effects modify the multiuser composite waveform. If a receiver model sums chip powers without resolving those effects, it can return a Q-factor that is too optimistic, and through that, a secrecy estimate that is too optimistic. Our estimates showed exactly that behaviour for high launch power. This is why the analytical, the SSFM, and the data-driven models are not treated as interchangeable in the present work. The analytical layer provides a transparent first estimate, while SSFM is utilized to address propagation and receiver timing. Moreover, calibration is constrained within the scope of the observed relationship, with the conclusive distance and power assertions derived from direct SSFM runs.

The work is structured into six technical contributions. First, the SA-SAC generator changes the global wavelength order and user order with key and time-index while preserving the disjoint supports. In addition, BER-derived channel capacities for Bob and Eve are analyzed along with the ILR. The SSFM receiver corrects chip delays per wavelength, but keeps uncompensated outputs for diagnostics. Fourth, all 27 base cases were rerun at $\mathrm{dz} \leq 0.125$ km, and only the 18 non-stress cases were used for operating-region calibration. Fifth, grouped validation was used when selecting the regression model, so neighbouring distance points were not treated as independent random samples. Finally, 14 distance cases and six power cases were simulated directly to bracket the reported limits. The implementation and data-processing steps were exercised by 132 unit and integration tests.

2. Related work and research gap

2.1 Recent SAC-OCDMA code and architecture development

Zero- and low-cross-correlation codes remain central to incoherent SAC-OCDMA because they reduce multi-access interference and phase-induced intensity noise. Recent examples include Pascal-triangle ZCC codes [4], polarization-assisted schemes [5,6], variable-weight designs [7], and two-dimensional optical orthogonal or spectral–spatial constructions [8,9]. Their objectives differ, but the usual comparison is based on cardinality, correlation, BER, receiver complexity, or supported user count. Once a code is selected, the wavelength assignment is typically fixed, and it is not usually considered as time-varying security parameter.

Studies of the channel still reveal that code performance is conditional on the propagation environment. SAC-based or OCDMA-based links have been studied within passive optical networks as well as in atmospheric and underwater optical channels [17–24]. Candidate designs can see a change in ranking due to turbulence, pointing error, water type, polarization, and code structure. These findings are pertinent here as they exclude a claim largely rooted in codes about security: the same mapping can give very different Bob and Eve observations following propagation and receiver processing.

2.2 Security and leakage of physical layer

Tan et al. [1] quantified a secure OCDMA architecture and pointed out the brute-force jeopardy of a small code space. Xu and colleagues [10] later demonstrated that information leakage of an OCDMA wiretap channel varies depending on tap location, link distance, confidential rate and optical code. Incidents of tapping, compromised elements, and other abnormal events at the physical layer introduces more risks on fiber infrastructures [2,3]. When all of these studies are combined so as to imply that BER at the legitimate receiver is not a right security descriptor. To create a meaningful claim, it is essential to state the Eve model, the allowed search effort, and the leakage measure used in the decision. None of the reviewed studies combines all the required elements for the current question, namely, a keyed SAC mapping, an explicit ILR condition, converged waveform-level fiber propagation, calibration limited to a validated operating range, group model validation, and direct measurements of the final distance and power ranges. The gap has method but no terminology. Mapping entropy is therefore reported here only as the size of the structural search space. The confidentiality claim is tied instead to Bob–Eve BER, secrecy capacity, and ILR, and the physical limits are taken from SSFM rather than from the surrogate model.

2.3 Machine learning in optical systems

Machine learning has been used to recognize SAC-OCDMA codes under changing weather conditions [12] and, more generally, to estimate quality of transmission, detect faults, and compensate impairments in optical systems [13–16,25–28]. The surveys in this area repeatedly identify limited data, model drift, weak interpretability, and optimistic validation as barriers to deployment [14,27,28]. A random split is especially questionable when nearby operating points from the same scenario appear in both training and test sets. We therefore compared leave-one-observation-out with leave-one-distance-out validation and based the uncertainty allowance on the larger residual scale. This choice made the model less flattering, but it provided a more honest indication of what the sparse dataset could support, Table 1 summarizes how the present workflow differs from representative code-design, security, propagation, and machine-learning studies.Table 1 appears here in the original manuscript and summarizes the critical positioning relative to representative recent work. The table compares the present study with the works of Tan et al. [1], Driz and Fassi [5], Xu et al. [10], Abd El-Mottaleb et al. [12], Kozdrowski et al. [13,25], and the present work across four dimensions: code/security contribution, propagation evidence, learning/optimization, and main limitation.

Table 1. Critical positioning relative to representative recent work.

Study	Code/security contribution	Propagation evidence	Learning/optimization	Main limitation relative to this work
Tan et al. [1]	Secure OCDMA architecture, secrecy analysis	Analytical/system model	No ML	No region-aware SSFM validation
Driz and Fassi [5]	2D spectral/polarization security and capacity	System simulation	No ML	No ILR-constrained operating map
Xu et al. [10]	Explicit ILR for OCDMA wiretap coding	Analytical/numerical	No ML	Security metric not embedded in SAC construction
Abd El-Mottaleb et al. [12]	ML-based SAC-OCDMA code recognition	FSO simulation	Code classification	No fiber nonlinearities or uncertainty-aware recommendation
Kozdrowski et al. [13,25]	QoT prediction in optical networks	Network datasets	Multiple ML models	Not specific to security-aware OCDMA
Present work	Keyed zero-cross-correlation SA-SAC; explicit ILR constraint	27-point full-resolution SSFM + convergence + 14 distance and 6 power points	Region calibration, grouped CV, ML-guided direct validation	Numerical validation only; one reference design

3. Proposed SA-SAC system and analytical model

Figure 1 illustrates the end-to-end security-aware analytical–SSFM–ML–direct-validation workflow. The figure shows the complete methodology from code generation through SSFM propagation to machine learning guidance and direct validation.

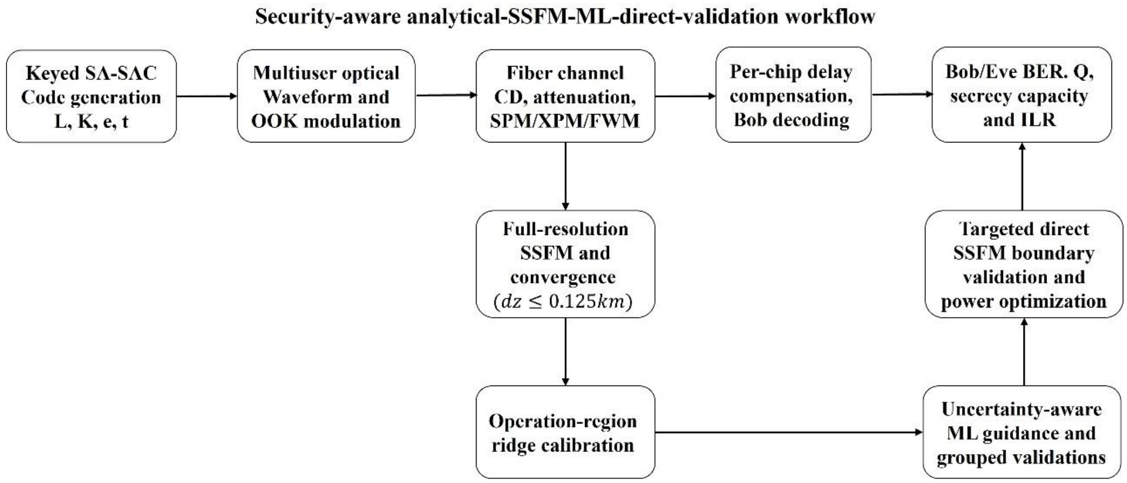

Fig. 1. End-to-end security-aware analytical–SSFM–ML–direct-validation workflow.

3.1 Constrained randomized code construction

Let $C(t)$ denote the $K \times L$ binary allocation matrix used in time slot t. Row k contains the wavelength chips assigned to user k. Each row must contain w_k active chips, and any two rows must have disjoint support:

$$\sum_{i=1}^{L} C_{k,i}(t) = w_k, \qquad C_i(t)C_j^T(t) = 0, \qquad i \neq j \qquad (1)$$

For a one-dimensional binary wavelength map, disjoint allocation is possible only when the total number of occupied chips does not exceed the available code length:

$$S = \sum_{k=1}^{K} w_k \leq L \qquad (2)$$

The generator first forms one key- and slot-dependent permutation of the wavelength indices. A second permutation determines the order in which users receive blocks from that wavelength list. The blocks are consecutive in the permuted domain and do not overlap. Randomising users independently would not provide the same guarantee, because two users could select the same chip. With the global construction, the transmitter and legitimate receiver reproduce the same map from the same secret and slot, whereas a change in slot produces a different valid allocation.

For labelled users with disjoint supports, the number of admissible wavelength assignments and its binary logarithm are:

$$N_{map} = \frac{L!}{(L-S)!\prod_{K=1}^{K} w_k!}, \qquad H_{map} = \log_2\left(N_{map}\right). \qquad (3)$$

The H_{map}indicates the degree of the admissible mapping set, but it will not serve as a proof of cryptographic security. In the reference case, $L = 64$, $K = 16$, $w = 4$ and $S = 64$. The matrix density $\text{laplace}((4,4), 0.0625)$, all wavelength chips are occupied and $H_{map} = 222.636\text{bits}$. Figure 2 illustrates a deterministic research realization produced from the public simulation seed. The figure shows a representative constrained SA-SAC code matrix where each user occupies four disjoint wavelength chips, giving $\lambda c = 0$. It exists to record the allocation rule and not for the purposes of exposing any operating key.

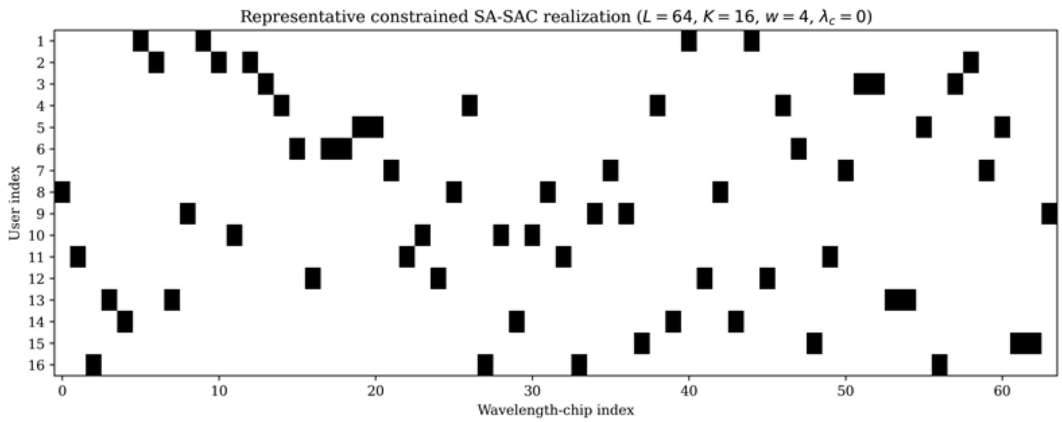

Fig. 2. Representative constrained SA-SAC code matrix. Each user occupies four disjoint wavelength chips, giving .

3.2 Bob–Eve receiver and security metrics.

Bob uses the current map to decode. It is assumed that Eve tests constant-weight candidates under a finite guessing budget, so the utility of her power depends on the overlap of a candidate with the active code. The detected levels for both receivers, the zero and the one, are mapped to the OOK Q-factor and the respective Gaussian BER approximation.

$$Q = \frac{\mu_1 - \mu_0}{\sigma_1 + \sigma_0} \ , \qquad BER = \frac{1}{2}\,\mathrm{erfc}\left(\frac{Q}{\sqrt{2}}\right) \ , \qquad (4)$$

The BER values are then mapped to binary-symmetric-channel capacities for Bob and Eve:

$$C_B = 1 - h_2(BER_B) \ , \qquad C_E = 1 - h_2(BER_E) \qquad (5)$$

$$C_s = \max(C_B - C_E, 0) \ , \qquad ILR = \max(R_s - C_s, 0) \qquad (6)$$

The secret code rate is established as . In this model, an implies that the secrecy capacity calculated can support this rate. It should not be interpreted to mean that all conceivable physical side channels have been extinguished. The OSF used an $ILR \le 0.05$ bit/symbol.

3.3 Fiber and impairment model

The analytical link model accounts for fiber attenuation, connector and decoder losses, finite extinction ratio, receiver shot noise, thermal noise, relative intensity noise, chromatic dispersion, and Kerr nonlinearities. The wavelength-dependent delay spread is approximated by $\Delta\tau = D\,\Delta\lambda\,L_f$. Nonlinear penalties are estimated from the effective length and γ through separate SPM, XPM, and FWM terms. Three cases were examined: standard SMF with $D = 17$ ps/nm/km and 100 GHz spacing, dense WDM with the same dispersion and 25 GHz spacing; and a low-dispersion case with $D = 2$ ps/nm/km and 25 GHz spacing. The nonlinear coefficient was 1.3 $W^{-1}\,km^{-1}$ in all three cases.

3.4 SSFM propagation and per-chip equalization

Waveform propagation was evaluated with the scalar lossy nonlinear Schrödinger equation and a symmetric split-step Fourier implementation:

$$\frac{\partial A(z,t)}{\partial z} = -\frac{\alpha}{2}A(z,t) - j\frac{\beta_2}{2}\frac{\partial^2 A(z,t)}{\partial t^2} + j\gamma|A(z,t)|^2\,A(z,t) \qquad (7)$$

Each spatial step applies half of the linear operator in the frequency domain, the nonlinear phase rotation in the time domain, and the remaining half of the linear operator. Because the multiuser field is propagated as a composite waveform, SPM, XPM, and FWM arise from the same field evolution rather than from three independent postprocessing penalties. At the receiver, every target wavelength is filtered separately, shifted by its calculated group delay, and then included in the square-law sum. The uncompensated path is retained as a diagnostic control.

3.5 Machine-learning guidance, region-aware calibration and direct validation

The 27 points of the base experiment include three launch powers ($-6, 4$ and $12\ \mathrm{dBm/user}$), three distances ($20, 50$ and $80\ \mathrm{km}$) and the three physical scenarios. The rerun employed a dz of no more than 0.125 km, 64 bits, spectral oversampling of 3 and a fixed seed. The operating region was formed by the rows -6 and $4\ \mathrm{dBm/user}$. The $12\ \mathrm{dBm/user}$ rows were kept because they reveal nonlinear failure, but they were excluded from the calibration fit. Ridge correction used the analytical Q-factor, total launch power, distance, and scenario indicators; the regularisation parameter was chosen by leave-one-out validation.

A second comparison included linear ridge, quadratic ridge, and Gaussian radial-basis-function kernel ridge models. For each model, the selection score was the larger of the leave-one-observation-out and leave-one-distance-out Q-RMSE values. The larger residual standard deviation was also used when forming the conservative Q bound. Candidate operating points had to satisfy both conditions below:

$$Q_{\mathrm{lower,95\%}} \geq 6 \quad \text{and} \quad \mathrm{ILR} \leq 0.05\,\frac{\mathrm{bit}}{\mathrm{symbol}} \qquad (8)$$

The lower bound admitted very few candidates, which was a consequence of sparse-data uncertainty rather than proof that the remaining distances were physically infeasible. The regression layer was therefore used as an experimental-design aid. The Direct Distance-Boundary Validation Frameworksimulated 14 additional points at 4 dBm/user to locate the last passing and first failing distance in 5 km increments. The Direct Boundary Power Optimization Framework added six runs at 2 and 3 dBm/user at those distances; together with the existing $4\ \mathrm{dBm/user}$ rows, these runs located the lowest tested passing power within 1 dB.

4. Numerical design and reproducibility

Table 2 presents the reference design and numerical parameters. The table lists all key parameters including code length ($\mathrm{L} = 64$ chips), users ($\mathrm{K} = 16$), weight ($\mathrm{w} = 4$ chips/user), data rate ($10\ \mathrm{Gb/s}$), center wavelength ($1550\ \mathrm{nm}$), attenuation ($0.2\ \mathrm{dB/km}$), nonlinear coefficient ($1.3\ \mathrm{W^{-1}\ km^{-1}}$), connector/decoder loss ($1/3\ \mathrm{dB}$), channel spacing (100 or 25 GHz), dispersion (17 or 2 $\mathrm{ps/nm/km}$), Eve tap fraction (0.01), extinction ratio (10 dB), responsivity (0.8 $\mathrm{A/W}$), dark current (1 nA), load/temperature (50 $\Omega/300$ K), RIN ($-155\ \mathrm{dB/Hz}$), operating powers (-6 and $4\ \mathrm{dBm/user}$), stress power ($12\ \mathrm{dBm/user}$), SSFM grid (27 full-resolution points), calibration rows (18 operating points), conservative final dz (0.125 km), bits/oversampling ($64/3$), random seed (20260712), and software tests ($132/132$ passed).

Table 2. Reference design and numerical parameters.

Parameter	Value	Parameter	Value
Code length L	64 chips	Users K	16
Weight w	4 chips/user	Data rate	10 Gb/s
Center wavelength	1550 nm	Attenuation	0.2 dB/km
Nonlinear coefficient γ	1.3 $\mathrm{W^{-1}\ km^{-1}}$	Connector/decoder loss	1/3 dB
Channel spacing	100 or 25 GHz	Dispersion	17 or 2 ps/nm/km
Eve tap fraction	0.01	Extinction ratio	10 dB
Responsivity	0.8 A/W	Dark current	1 nA
Load/temperature	50 Ω / 300 K	RIN	−155 dB/Hz
Operating powers	−6 and 4 dBm/user	Stress power	12 dBm/user

SSFM grid	27 full-resolution points	Calibration rows	18 operating points
Conservative final dz	0.125 km	Bits/oversampling	64 / 3
Random seed	20260712	Software tests	132/132 passed

Every point in the 27-case grid was propagated with $dz \le 0.125$ km, 64 bits, and spectral oversampling of 3. Depending on distance and sampling requirements, a run used as many as 640 spatial steps and 131072 temporal samples. A fixed-pattern convergence check compared the operating result with a 0.0625 km step where the 0.125 km setting required confirmation. The 12 dBm/user cases were retained as stress diagnostics because both their analytical mismatch and their step sensitivity were markedly larger than those observed at −6 and 4 dBm/user. The numerical settings used for the Direct Distance-Boundary Validation Framework and the Direct Boundary Power Optimization Framework boundary runs were the same. Deterministic seeds, saved checkpoints, completion manifests, and 132 passing software tests ensured reproducibility.

5. Results

5.1 The security nature is important.

Each of the sixteen rows of the reference code had weight four, and any pair of rows had a overlap of zero. Since $Kw = L$, the allocation uses all 64 wavelength chips and ensures no chip is assigned to more than one user. When the same key and slot were repeated, the same matrix was reproduced by the KHS. When the slot was changed, the wavelength and user permutations changed; however, the constraints were preserved. Mapping entropy was calculated to be 222.636 bits. Bob decoded successfully with the correct allocation, while Eve's limited searches yielded partial outcomes. At the final three operating points, the adopted $R_s = 0.9\text{bit/symbol}$ model gave an ILR = 0. This result is for the stated Eve model and confidential rate.

5.2 Delay compensation and SSFM behavior

Figure 3 shows the controlled receiver diagnostic showing the effect of wavelength-dependent per-chip delay compensation at 20 km and 4 dBm/user.

The figure demonstrates the dramatic improvement in Q-factor and BER when per-chip delay compensation is applied.

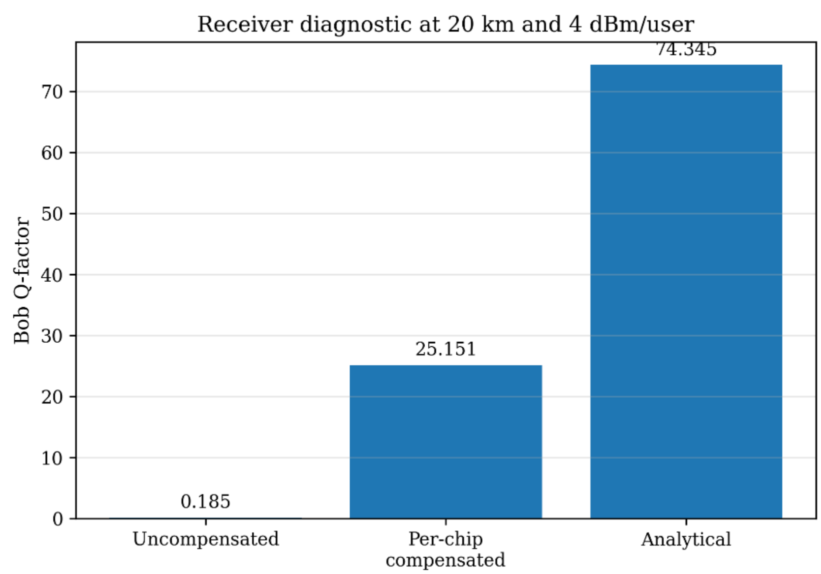

Fig. 3. Controlled receiver diagnostic showing the effect of wavelength-dependent per-chip delay compensation at 20 km and 4 dBm/user.

The receiver diagnostic exposed a timing problem that is hidden by a chip-power-only calculation. At 20 km in standard SMF with 100 GHz spacing, the target chips accumulated 817.42 ps of relative delay, equivalent to about 8.17 bit periods at 10 Gb/s. Without delay correction, Bob's Q-factor was 0.18525 and the BER was 0.42652.

Aligning the chips before square-law detection increased Q to 25.1513 and reduced the computed BER to 6.84×10^{-140}. The analytical model predicted $Q = 74.3453$. Thus, equalization repaired the dominant timing error but did not reproduce the waveform result predicted by the simpler model.

Table 3 presents the controlled diagnostic effect of per-chip delay equalization at 20 km in standard SMF. The table compares uncompensated, compensated, and analytical results for Bob Q-factor, Bob BER, differential chip delay, received one-level power, and spectral broadening factor. The uncompensated BER, which is close to random detection, shows that the proposed decoder requires chip-level synchronization or an equivalent dispersion-management function.

This controlled case was used to isolate the receiver-timing mechanism. It was not used to set the distance or power limits; those claims come from the independently rerun full-resolution validation and boundary optimization framework.

Table 3. Controlled diagnostic effect of per-chip delay equalization at 20 km in standard SMF.

Metric	Uncompensated	Compensated	Analytical
Bob Q-factor	0.18525	25.1513	74.3453
Bob BER	0.42652	6.84×10^{-140}	≈0 (numerical floor)
Differential chip delay	817.42 ps	817.42 ps	Included as penalty
Received one-level power	—	−4.112 dBm	—
Spectral broadening factor	—	1.0156	—

This controlled case was used to isolate the receiver-timing mechanism. It was not used to set the distance or power limits; those claims come from the independently rerun Full-Resolution Validation and Boundary Optimization Framework. The uncompensated BER, which is close to random detection, shows that the proposed decoder requires chip-level synchronization or an equivalent dispersion-management function.

5.3 Nonlinear stress and operating-domain separation

At 12 dBm/user, the 16-user launch power was 24.041 dBm, or approximately 0.253 W in total. The nine stress points produced a Q-RMSE of 55.025 and a Q-MAE of 27.058 for the raw analytical model; $Q - R^2$ fell to -807.18 and log10(BER)-RMSE reached 9.9783. Applying the operating-region correction outside its fitted domain reduced the Q error but did not make the model credible: Q-RMSE remained 21.345 and $Q - R^2$ was -120.62. These rows therefore serve as evidence of model breakdown under nonlinear stress, not as calibration samples or recommended operating points.

5.4 SSFM convergence

Table 4 presents targeted SSFM convergence evidence. The table shows for each scenario (standard SMF, dense WDM, low dispersion) the user power (P_{user} in dBm), length L in km, dz pair in km, ΔQ in %, ΔlogBER, ΔP in dB, and convergence status. The operating cases satisfied the stated convergence limits: $\Delta Q \leq 5\%$, $\Delta \log10(BER) \leq 0.5$,an $\Delta P \leq 0.25$ dB . Standard SMF was additionally checked at 0.0625 km ,the Q-factor changed by only 0.0965% between 0.125 and 0.0625 km. For dense WDM and the low-dispersion operating case, the 0.25-to-0.125 km comparison was also within tolerance. The two high-power checks did not converge under the same criteria, which is consistent with their treatment as diagnostic stress cases.

Table 4. Targeted SSFM convergence evidence.

Scenario	Puser (dBm)	L (km)	dz pair (km)	ΔQ (%)	ΔlogBER	ΔP (dB)	Converged
Standard SMF	4	50	0.125/0.0625	0.096	0.000	0.039	Yes
Dense WDM	4	50	0.25/0.125	2.374	0.440	0.053	Yes

Low Dispersion	4	50	0.25/0.125	2.201	0.000	0.062	Yes
Dense WDM	12	50	0.125/0.0625	23.606	4.038	0.470	No
Low Dispersion	12	50	0.125/0.0625	9.825	3.255	0.180	No

5.5 Operating-region calibration

Figure 4 shows the full-resolution operating-region errors before and after ridge calibration. The figure compares the raw analytical errors with the calibrated errors for both Q-factor and logBER metrics.

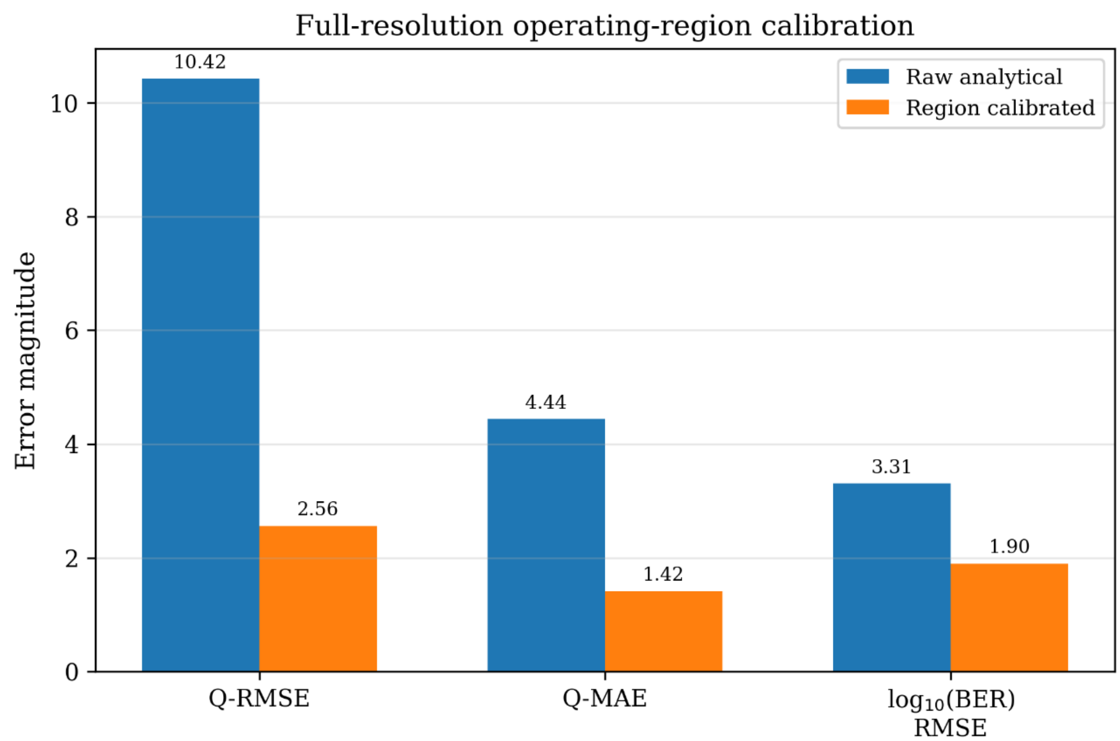

Fig. 4. Full-resolution operating-region errors before and after ridge calibration.

Table 5 presents the full-resolution region-aware calibration performance. The table shows for the operating region (raw analytical and calibrated) and stress region (raw analytical and calibrated extrapolation) the number of samples , Q-RMSE, Q-MAE, Q-R^2, logBER RMSE, and logBER R^2.

Table 5. Full-resolution region-aware calibration performance.

Region	Model	n	Q-RMSE	Q-MAE	Q-R^2	logBER RMSE	logBER R^2
Operating	Raw analytical	18	10.421	4.4435	−0.39044	3.3092	0.82935
Operating	Calibrated	18	2.5624	1.4163	0.91594	1.9011	0.94368
Stress	Raw analytical	9	55.025	27.058	−807.18	9.9783	−2.8428
Stress	Calibrated extrapolation	9	21.345	12.497	−120.62	7.6749	−1.2734

The operating-region correction materially changed the agreement with SSFM. Q-RMSE fell from 10.421 to 2.5624, a reduction of 75.4%, and Q-MAE fell from 4.4435 to 1.4163. $Q - R^2$ moved from -0.39044 to 0.91594. For $\log - \mathrm{BER}, R^2$ increased from 0.82935 to 0.94368.

The mean signed Q error after calibration was -0.3241, indicating a small conservative shift. These gains apply to the 18 operating rows used to define the domain. The remaining stress errors are a reminder that the fitted correction should not be interpreted as a global nonlinear channel model.

5.6 Machine-learning validation

Figure 5 shows the validation statistics for the selected quadratic-ridge surrogate. The figure presents LOOCV and leave-one-distance-out validation results.

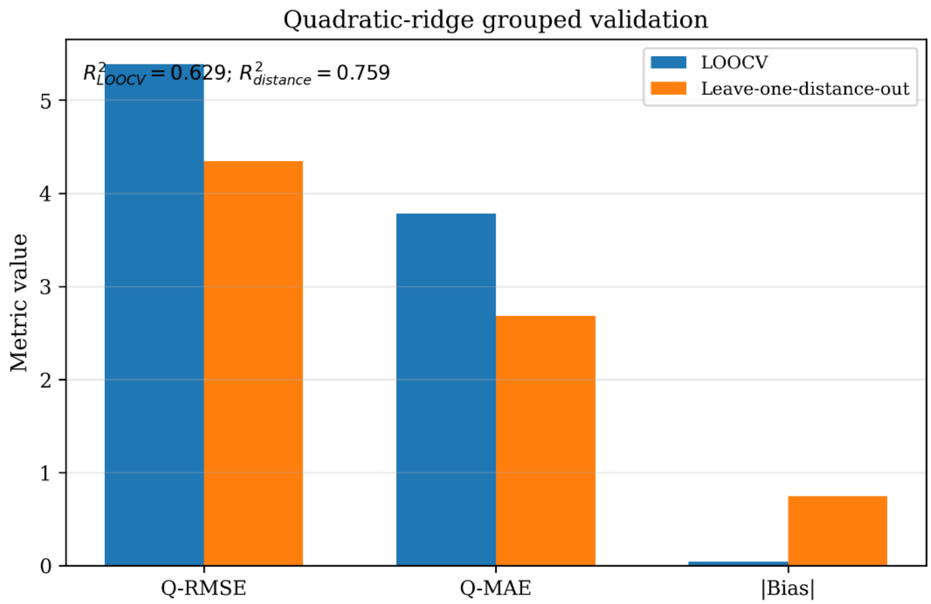

Fig. 5. Validation statistics for the selected quadratic-ridge surrogate.

Using the worst grouped-validation score, quadratic ridge regression with $\lambda = 0.001$ was selected. Under leave-one-observation-out validation, Q-RMSE was 5.3855, Q-MAE was 3.7825, and R^2 was 0.62867. Holding out complete distances gave Q-RMSE $=$ 4.3427, Q-MAE $=$ 2.6811, and $R^2 = 0.75854$. The conservative residual standard deviation was 5.5416 Q units, so the nominal 95% subtraction was approximately 10.86 Q units. That interval is deliberately severe; it reflects how little independent structure is available in an 18-point operating dataset.

Table 6 presents the validation performance of the selected machine-learning model. The table shows LOOCV, leave-one-distance-out, selection score, and conservative residual SD metrics.

Table 6. Validation performance of the selected machine-learning model.

Validation	Q-RMSE	Q-MAE	Q-R²	Bias
LOOCV	5.3855	3.7825	0.62867	0.03966
Leave-one-distance-out	4.3427	2.6811	0.75854	−0.74475
Selection score	5.3855	—	—	—
Conservative residual SD	5.5416	—	—	—

Only five of the 39 scenario–distance candidates passed the lower-95% Q requirement. The resulting confidence-qualified map stopped at 40 km for standard SMF and did not certify a positive distance for dense WDM or the low-dispersion case. Direct simulations later showed that both links could operate beyond those apparent limits. The discrepancy is best interpreted as uncertainty from limited training coverage, not as physical failure. Consequently, the model was used to decide where another SSFM run would be useful, and not to publish the boundary itself.

5.7 Direct SSFM distance-boundary validation

Figure 6 shows the direct SSFM distance-boundary brackets at 4 dBm/user. Bars show the last feasible distance and upper whiskers the first infeasible distance for standard SMF, dense WDM, and low-dispersion cases.

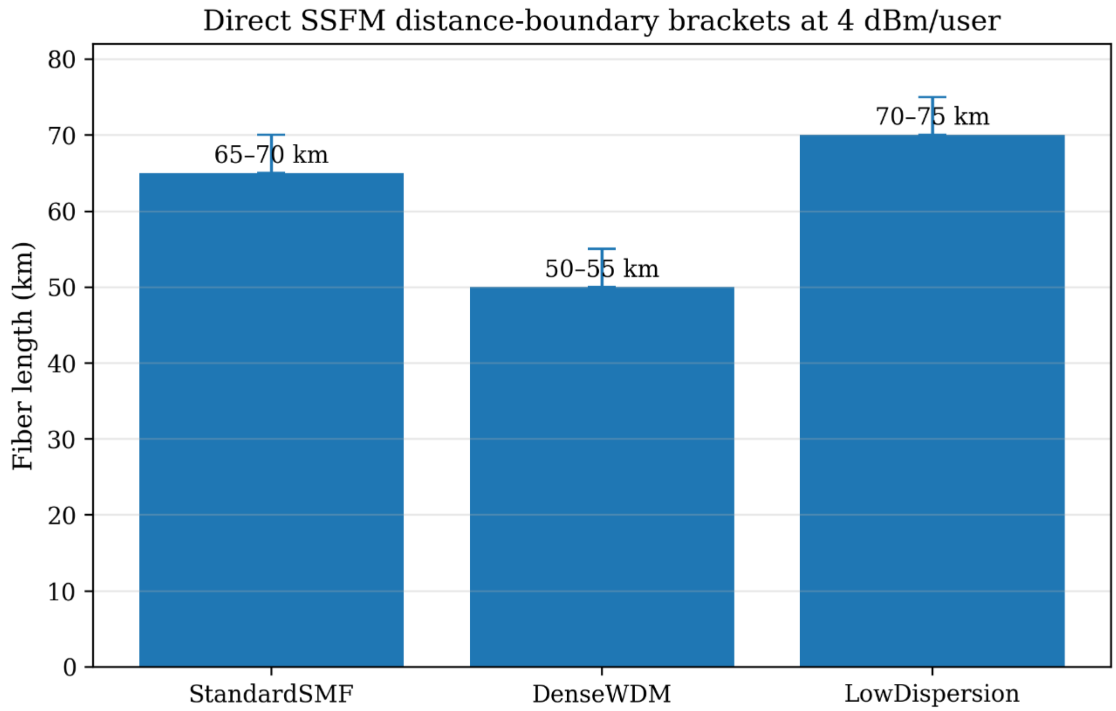

Fig. 6. Direct SSFM distance-boundary brackets at 4 dBm/user. Bars show the last feasible distance and upper whiskers the first infeasible distance.

The Direct Distance-Boundary Validation Framework evaluated 14 SSFM points at $4\,\mathrm{dBm/user}$ and combined them with the corresponding base-grid rows. Standard SMF passed at 65 km and failed at 70 km. Dense WDM passed at 50 km and failed at 55 km. The low-dispersion case passed at 70 km and failed at 75 km. The Q-factors at the last passing points were 6.3786, 6.4259, and 6.8981, respectively. All three points also met the ILR $\leq 0.05\,\mathrm{bit/symbol}$ condition, with calculated ILR $= 0$.

Table 7 presents the directly bracketed reliable-and-secure distance boundaries at 4 dBm/user. The table shows for each scenario the last feasible distance (km), first infeasible distance (km), bracket (km), Q at boundary, BER at boundary, and ILR.

Table 7. Directly bracketed reliable-and-secure distance boundaries at 4 dBm/user.

Scenario	Last feasible (km)	First infeasible (km)	Bracket (km)	Q at boundary	BER at boundary	ILR
Standard SMF	65	70	65–70	6.3786	8.9381e−11	0
Dense WDM	50	55	50–55	6.4259	6.5567e−11	0
Low Dispersion	70	75	70–75	6.8981	2.6343e−12	0

These direct brackets supersede the preliminary limits suggested by the regression model. Dense WDM reached the shortest distance, which is consistent with the stronger interaction expected when the channel spacing is reduced to . The low-dispersion link reached the farthest tested distance because wavelength-dependent walk-off was smaller in the operating region. The simulations were spaced by , so the evidence supports brackets of , and rather than an untested continuous value inside each interval.

5.8 Direct boundary-power optimization

Figure 7 shows the direct SSFM Bob Q compared to user launch power experienced at the established distance boundary for each scenario. The figure demonstrates the Q-factor performance at the boundary distances for powers of 2, 3, and 4 dBm/user.

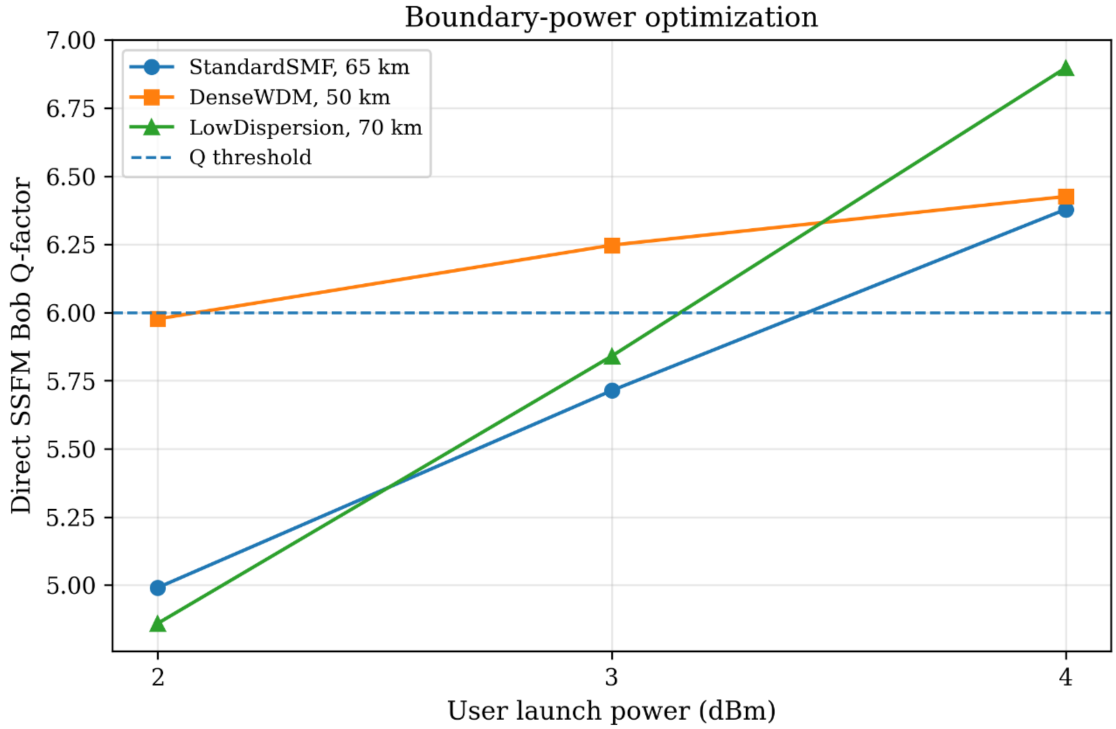

Fig. 7. shows the direct SSFM Bob Q compared to user launch power experienced at the established distance boundary for each scenario.

The Direct Boundary Power Optimization Framework evaluated launch powers of2 and 3 dBm/user at all existing distance points and combined the results with the existing 4 dBm/user point. The standard SMF failed at lower powers at 65 km while it passed at 4 dBm/user. The Dense WDM at 50 km was just above the threshold at 2 dBm/user ($Q = 5.9764$) and passed at 3 dBm/user($Q = 6.2473$) . The low-dispersion link failed at 2 and 3 dBm/user but passed at 4 dBm/user a 70 km . The lowest tested passing powers therefore were 4, 3, and 4 dBm/user.

Table 8 presents the direct boundary-power optimization results. The table shows for each scenario the distance (km), selected power (dBm/user), power bracket (dBm/user), Q, BER, and total launch power (dBm). The values are discrete experimental minima within a 1 dB search, not continuously optimized powers. All of the chosen points had ILR = 0 in the selected model. The one decibel lower power required per user for dense WDM was achieved at the shorter boundary 50 km. The case representing the lowest possible dispersion showed the longest validated distance, largest boundary Q-factor and the lowest BER.

Table 8. Direct boundary-power optimization results.

Scenario	Distance (km)	Selected power (dBm/user)	Power bracket (dBm/user)	Q	BER	Total launch power (dBm)
Standard SMF	65	4	$3 < Pmin \leq 4$	6.3786	8.9381e−11	16.041
Dense WDM	50	3	$2 < Pmin \leq 3$	6.2473	2.0885e−10	15.041
Low Dispersion	70	4	$3 < Pmin \leq 4$	6.8981	2.6343e−12	16.041

6. Discussion

6.1 Security and performance must be designed together.

Zero cross-correlation provides a solution to interference allocation issues, but it doesn't guarantee confidentiality by itself. From recurring observations, one may still conclude a fixed ZCC pattern. Also, a high Q-factor at Bob says nothing about what Eve could decode. The allocation changes with key and time slot in SA-SAC construction keeping the spectral supports disjoint. The extra ILR requirement rules out acceptance of a reliable-but-leaky point under the said wiretap model. The high-power rows also indicate why a security decision cannot be separated from propagation. Over there, while the analytical Q-factor still looked good, the directly propagated waveform began to worsen. Any optimizer driven solely by either the received power or the analytical Q would therefore be capable of determining an unsupported point. Keeping the separation between interpolation and extrapolation clear, 12 dBm/user cases are segregated from the fitted operating region.

6.2 The significance of timing equalization at chip level.

One bit occupies 100 ps at 10 Gb/s. As a result, the 817 ps measured chip-to-chip delay, after only 20 km, is no small correction, being more than eight-bit periods long. This is the reason for the nearly random uncompensated BER as shown in Table 3. Design analysis using SAC-OCDMA summing spectral-chip powers while ignoring timing can miss failure mode. In the indicated configuration the wavelength-specific alignment or dispersion-management method as physically equivalent is incorporated in the receiver rather than a choice refinement.

6.3 The value and limits of calibration and machine learning.

The calibration outcome shown in Table 5 and Figure 4 demonstrates that a basic modification can link a less expensive simple transparent analytical model to a more expensive propagation model with stated operational domain. The sufficiency does not demonstrate a single formula valid over the full nonlinear range. In two of the three scenarios, the grouped-validation errors and 5.5416-Q residual scale were also too large to justify final boundary claims as shown in Table 6. It is crucial to keep those unfavorable statistics as a random split would have mixed neighboring physical conditions and resulted in a less informative estimate. Machine learning had a useful but limited role in this workflow. The search was subsequently narrowed to operating points with the greatest potential to influence the simulation outcomes. Evidence obtained from the direct distance-boundary validation (Figure 6 and Table 7) and boundary power optimization analyses (Figure 7 and Table 8) was used to define the reported operating boundaries. It is less objectionable to treat this labor division as a more general optimizer in a 18-point surrogate. The model that has been trained will remain specific to $L = 64$, $K = 16$, $w = 4$, the three studied scenarios and the sampled power region.

6.4 Directly validated operating limitations.

The last three points (Table 8) represent different engineering compromises. The 70 km low-dispersion case was achieved due to reduced wavelength walk-off preserving the waveform at the power tested. Standard SMF reached sixty-five km. Dense WDM was limited to 50 km due to tighter spectral spacing, but crossed the reliability threshold at 3 dBm/user instead of 4 dBm/user. By reporting a distance interval of 5 km and power interval of 1 dB we do not imply a resolution that was not simulated and leave clear targets for laboratory refinement.

6.5 Comparison with recent work

Compared with secure OCDMA and ILR studies [1,5,9,10], the added evidence here is the converged waveform-level propagation and the direct bracketing of both distance and power. Compared with machine-learning work on code recognition and optical quality of transmission [12–16,25–29], grouped validation is followed by new SSFM runs rather than being treated as the end of the analysis. Compared with recent code-construction studies [4–9,30], the wavelength assignment is time dependent and the mapping search space is kept conceptually separate from measured leakage. The proposed layer is therefore complementary to conventional cryptography, not a replacement for it.

7. Limitations and future work

The study is numerical. The scalar SSFM does not represent polarization-mode dispersion, polarization coupling, Raman effects, accumulated amplifier spontaneous-emission noise, device drift, or non-ideal laboratory receiver components. Although the 27 base cases were rerun with $dz \leq 0.125$ km and the boundary points were simulated directly, the search increments were 5 km in distance and 1 dB in launch power. A finer numerical or experimental claim would require additional samples inside the reported brackets.

The bounds of the security calculation are specified. This paper derives the ILR as a function of a binary-symmetric-channel approximation and a finite-search Eve model. The data-driven part utilizes one code design ($\mathrm{L} = 64, \mathrm{K} = 16, \mathrm{w} = 4$), three physical scenarios, and a limited operational power range. Due to these selections, generalization to other code weights, user loads and hardware will be limited. A wider study should produce complete code and channel designs during validation and should assess Bob and Eve from received samples rather than just from BER-derived capacities.

Future research should investigate adaptive Eve receivers and estimate mutual information directly from the detected waveforms. This hardware implementation will also require measuring the wavelength-reconfiguration latency, key distribution and synchronization overhead, and decoder tolerances. Experimental co-validation must include genuine path and tapped path. By depositing the seeds, SSFM settings, processing scripts, and machine-readable tables in a permanent archive it will allow others to reproduce or contest the operating brackets.

8. Conclusion

The main result of this work is not a universal closed-form limit, but a verified procedure for moving from a security-aware SAC allocation to defensible optical operating brackets. The keyed allocation preserved zero pairwise overlap for the $64 - chip$, 16-user reference design. Full-resolution SSFM showed that wavelength-dependent chip alignment was necessary and that the analytical approximation became unreliable in the 12 $dBm/user$ stress region. Within the $18 - point$ operating region, ridge calibration reduced Q-RMSE from 10.421 to 2.5624 and raised $Q - R^2$ to 0.9159as shown in Table 5. The quadratic-ridge model helped select additional simulations, but its uncertainty was not used as final physical evidence. Direct SSFM placed the last tested secure-and-reliable points at 65 km and 4 $dBm/user$for standard SMF, 50 km and 3 $dBm/user$ for dense WDM, and 70 km and 4 $dBm/user$ for the low-dispersion case. Their Q-factors were 6.3786,6.2473, and 6.8981, respectively, with $ILR = 0$ under the adopted model. These values should be read together with the reported 5 km distance and 1 dB power brackets.

References

1. Y. Tan, T. Pu, H. Zhou, J. Zheng, G. Su, J. Liu, Design and performance analysis of a novel secure communication system based on OCDMA, Optical Fiber Technology 58 (2020) 102254.
2. V. Spurny et al., Physical layer components security risks in optical fiber infrastructures, Sensors 22 (2022) 588.
3. M. Ruzicka et al., Classification of events violating the safety of physical layers in fiber-optic network infrastructures, Sensors 22 (2022) 9515.
4. S. Driz, B. Fassi, C. Kandouci, F. Ghali, Performance improvement of a novel zero cross-correlation code using Pascal's triangle matrix for SAC-OCDMA systems, Opto-Electronics Review 30 (2022) e140550.
5. S. Driz, B. Fassi, Enhancing QS-SAC-OCDMA system capacity and security using two-dimensional spectral/polarization OZCZ codes, Optical and Quantum Electronics (2022).
6. S.M. Ammar et al., Development of new spectral amplitude coding OCDMA code by using polarization encoding technique, Applied Sciences 13 (2023) 2829.
7. Z. Lu, Y. Lu, C. Li, Design of zero cross correlation variable weight codes for multimedia services based on magic square in SAC-OCDMA systems, Optoelectronics Letters 17 (2021) 539–545.
8. M. Shao, X. Niu, Construction of optimal two-dimensional optical orthogonal codes with at most one pulse per wavelength, Entropy 26 (2024) 741.
9. R. Ullah et al., Optimization and analysis of spectral/spatial OCDMA passive optical network, AEU—International Journal of Electronics and Communications 175 (2024) 155084.
10. R. Xu, L. Sun, J. Ji, K. Wang, Y. Song, Information leakage rate of optical code division multiple access network using wiretap code, Entropy 25 (2023) 1384.
11. A.M. Alhassan et al., Performance Analysis of Coherent Source SAC OCDMA in Free Space Optical Communication Systems, Symmetry 15 (2023) 1152.
12. S.A. Abd El-Mottaleb, A. Métwalli, M. Singh, M. Hassib, M.H. Aly, Machine learning FSO-SAC-OCDMA code recognition under different weather conditions, Optical and Quantum Electronics 54 (2022) 851.
13. S. Kozdrowski et al., Machine learning algorithms for prediction of the quality of transmission in optical networks, Entropy 23 (2021) 7.
14. G. Villa, C. Tipantuña, D.S. Guamán, G.V. Arévalo, B. Arguero, Machine learning techniques in optical networks: a systematic mapping study, IEEE Access 11 (2023) 98714–98750.
15. D. Wang, X. Jiang, Y. Song, Physics-informed machine learning for optical fiber communications: opportunities and challenges, in: Proc. OECC, 2023.

16. J. Uduagbomen et al., Physics-informed neural network for fibre channel modelling in optical communication systems, in: Proc. ICTON, 2023.
17. M.M. Al Hammadi, M.J. Islam, Performance evaluation of underwater wireless optical CDMA system for different water types, Photonic Network Communications 39 (2020) 246–254.
18. M.J. Islam, B. Mitra, Performance analysis of 2D WH/TS OCDMA system through atmospheric turbulence channel, Optical and Quantum Electronics 53 (2021) 224.
19. B. Mitra, M.J. Islam, Effect of adverse weather conditions and pointing error on the performance of 2-D WH/TS OCDMA over FSO link, Journal of Optical Communications (2020).
20. N. Das, M.J. Islam, Influence of different codes on the performance of SAC-OCDMA over FSO link, International Journal of Communication Systems 37 (2024) e5701.
21. A. Armghan, M. Alsharari, K. Aliqab, M. Singh, S.A. Abd El-Mottaleb, Performance analysis of hybrid PDM-SAC-OCDMA-enabled FSO transmission using ZCC codes, Applied Sciences 13 (2023) 2860.
22. M. Singh et al., Performance analysis of 6 × 10 Gbps PDM-SAC-OCDMA-based FSO transmission using EDW codes with SPD detection, Optik 264 (2022) 169415.
23. M. Singh et al., 6G network architecture using FSO-PDM/PV-OCDMA system with weather performance analysis, Applied Sciences 12 (2022) 11374.
24. R. Ullah et al., An optimized architecture to reduce the impact of fiber strands in spectral/spatial optical code division multiple access passive optical networks (OCDMA-PON), Optical Fiber Technology 54 (2020) 102072.
25. S. Kozdrowski et al., A Comprehensive Study of Machine Learning Application to Transmission Quality Assessment in Optical Networks, Applied Sciences 13 (2023)4657.
26. X. Chen, J.E. Hurley, J.S. Stone, M.-J. Li, Chromatic dispersion measurements of single-mode, polarization-maintainingFibers, and few-mode fibers using a frequency-domain method, Photonics 10 (2023) 215.
27. C. Shao et al., Machine learning in short-reach optical systems: a comprehensive survey, Photonics 11 (2024) 613.
28. Z. Xu et al., Advanced neural-network-based equalization in IM/DD optical systems: current status and future trends, Photonics 11 (2024) 702.
29. M.A. Amirabadi, S.A. Nezamalhosseini, M.H. Kahaei, L.R. Chen, A comprehensive survey on machine and deep learning for optical communications, IEEE Access 13 (2025) 88794–88846.
30. R. Ullah et al., Fault tolerant spectral/spatial optical code division multiple access passive optical network, Sensors 24 (2024) 7355.
31. S.A. Abd El-Mottaleb et al., OCDMA transmission-based underwater wireless optical communication system: performance analysis, Optical and Quantum Electronics 55 (2023) 465.